PHYSICS AND CHEMISTRY OF SOLID STATE
V. 27, No. 1 (2026) pp. 206-214
Section: Technology

DOI: 10.15330/pcss.27.1.206-214

Vasyl Stefanyk Carpathian National University

ФІЗИКА І ХІМІЯ ТВЕРДОГО ТІЛА
Т. 27, № 1 (2026) С. 206-214
Технічні науки

UDK: 621.791:669.24:539.374

ISSN 1729-4428 (Print)
ISSN 2309-8589 (Online)

V.V. Usov[1], N.M. Shkatulyak[1], S.I. Iovchev[2], D.V. Pavlenko[3], D.E. Molochkov[3], R.A. Kulikovsky[3]

Elastic Property Anisotropy in Inconel 718 Alloy Specimens Fabricated by Wire Arc Additive Manufacturing

[1]South Ukrainian National Pedagogical University named after K. D. Ushynsky, Odesa, Ukraine;
[2]Odesa National Maritime University, Odesa, Ukraine;
[3]National University "Zaporizhzhia Polytechnic", Zaporizhzhia, Ukraine, dvp1977dvp@gmail.com

This study investigates the anisotropy of elastic properties in Inconel 718 alloy specimens fabricated via Wire Arc Additive Manufacturing (WAAM). The crystallographic texture of the specimens was characterized using inverse pole figures (IPF) obtained in three mutually orthogonal directions: the build direction (along the layer deposition), the transverse direction (the scanning direction), and the normal direction (perpendicular to both build and transverse directions). The analysis revealed that the texture is well-described by a combination of ideal orientations with some degree of dispersion. Based on the elastic constants of Inconel 718 single crystals and the pole density data derived from the IPF, the Young's modulus, shear modulus, and Poisson's ratio were calculated for each of the three orthogonal directions. The results demonstrate that the Young's modulus in the normal direction is, on average, 10-11% lower than in the build and transverse directions. Conversely, the shear modulus and Poisson's ratio exhibit higher values in the normal direction. The study concludes that crystallographic texture is the dominant factor contributing to the observed anisotropy in the mechanical properties of the WAAM-fabricated Inconel 718 specimens. Therefore, strategic control of crystallographic texture during WAAM processing offers a pathway to engineer components with a tailored, optimized combination of mechanical properties.

Keywords: wire arc additive manufacturing, crystallographic texture, heat-resistant Inconel 718 alloy, inverse pole figures, anisotropy.

Receive 29 June 2025; Accepted 05 February 2026; Published 30 March 2026.

Introduction

The aerospace industry has recently shown increasing interest in exploring and implementing novel, promising manufacturing methods for components [1], with a particular focus on additive manufacturing (AM) technologies [2]. Among the various AM methods categorized by the ISO/ASTM 52900:2021 standard [3], Directed Energy Deposition (DED) technology is experiencing growing adoption. DED utilizes focused thermal energy, typically from a laser, electron beam, or plasma arc, to fuse materials by melting them as they are deposited. DED processes are known for their high productivity [4]. Furthermore, DED technology can be applied to the repair and modification of existing components [5].

Among DED technology variants, WAAM is considered one of the most accessible and cost-effective. WAAM integrates two established manufacturing processes: gas metal arc welding and additive manufacturing. The WAAM process utilizes an electric arc as its heat source [6]. This arc is generated between a continuously-fed consumable wire electrode and the substrate, melting both to create a weld pool. The wire therefore serves a dual function: it acts as the electrode, sustaining the arc, while simultaneously providing the feedstock material for deposition.

Using wire as the feedstock material offers several advantages over powder-based additive manufacturing methods. The material feed system is simplified in design, localized shielding of the build area becomes feasible, and cost savings can be realized due to the wider availability

and simpler manufacturing process of wire. Furthermore, the use of wire feedstock eliminates the occupational health and safety concerns associated with the dispersion of fine metallic powder particles into the atmosphere.

The high deposition rates achievable with WAAM (typically ranging from 4 to 10 kg/hour), combined with the ability to fabricate large-scale and geometrically complex metal components from readily available, weldable materials in wire form [7], position it as a promising technique for aerospace component manufacturing.

Among heat-resistant alloys, Inconel 718 is widely employed in the energy and aerospace industries due to its exceptional combination of mechanical properties, including high yield and tensile strength, as well as good fatigue and creep resistance [8]. Because Inconel 718 is a critical yet expensive material used extensively across various industrial sectors, cost-effective production methods are required to minimize processing costs and material waste, improve design efficiency, and reduce lead times. WAAM has the potential to significantly reduce both manufacturing time (by more than 40%) and post-processing time (by more than 15%) compared to other AM methods, with the degree of improvement dependent on component size [9].

Despite the growing popularity of the WAAM process, the technology has limitations stemming from the need for mechanical post-processing of manufactured component surfaces. These surfaces exhibit geometric inhomogeneities, which deviate from the intended product geometry and increase material consumption during subsequent machining. According to [10], these form inhomogeneities originate from a combination of factors: crystal structure defects, microstructural variations, surface roughness and waviness, and deviations in overall product shape and position. The latter three—surface roughness, waviness, and shape/position deviations—are the primary geometric inhomogeneities necessitating mechanical post-processing. Research [11] indicates that the principal cause of these surface imperfections in WAAM-produced components is the significant temperature gradient that develops during the deposition process. This gradient induces residual thermal stresses, both macro and micro, ultimately leading to deviations from the desired product geometry [11].

Numerous publications focus on investigating the technical conditions required to mitigate form defects in WAAM-produced components by reducing thermal stresses. These efforts primarily involve optimizing the WAAM process parameters and improving the control of temperature and heat input during manufacturing [12].

Several studies have indicated that the mechanical properties of components fabricated via WAAM can exhibit anisotropy. Specifically, it has been observed that the elastic characteristics and strength parameters of austenitic steel in the transverse direction (across layers) are lower than those in the longitudinal direction (along the deposition path) due to the uneven surface [13, 14].

Research [15] demonstrated that 308LSi austenitic stainless-steel specimens produced using WAAM exhibit a pronounced anisotropy in both microstructure and mechanical properties. This anisotropy is attributed to the formation of a well-defined crystallographic texture during the layer-by-layer material deposition process.

Accurate determination of material elastic parameters is fundamental for reliable evaluation of product strength characteristics, as confirmed by research [16]. The WAAM manufacturing process creates specific crystallization conditions, leading to the formation of preferential crystallite orientation in the metal matrix [17]. As a result, the elastic properties of the material acquire macroscopic anisotropy, significantly affecting the operational characteristics of products.

The accurate determination of a material's elastic parameters is fundamental for the reliable evaluation of a product's strength characteristics, as research has confirmed [16]. The WAAM manufacturing process creates unique crystallization conditions, which promote the formation of a preferential crystallographic orientation (texture) within the metal matrix [17]. Consequently, the material's elastic properties exhibit macroscopic anisotropy, significantly impacting the operational performance of manufactured components.

To effectively leverage the potential benefits of this anisotropy in structural design, it is crucial to develop and validate methodologies for both predicting and experimentally determining elastic parameters. These methodologies must account for the influence of technological factors on the resulting texture formation. Particular attention should be directed towards the elastic modulus, as this parameter directly influences the accuracy of stress state calculations within the material. Employing averaged values of the elastic modulus across all structural elements can introduce significant errors in stress-strain state analysis and, consequently, lead to inaccurate determination of the safety factor.

The objective of this study is a comprehensive analysis of the anisotropy of the elastic and shear moduli, as well as Poisson's ratio, in Inconel 718, a heat-resistant nickel alloy, specimens. These specimens were fabricated using WAAM technology and subsequently underwent surface finishing via grinding. The determination of these properties was performed using a combination of single-crystal elastic constants and texture parameters obtained through X-ray diffractometry.

I. Materials and Methods

Specimens were fabricated from a nickel-based, heat-resistant Inconel 718 alloy (composition: Cr: 17.0-21.0; Ni: 50.0-55.0; Mo: 2.8-3.3; Nb: 4.75-5.50; Ti: 0.65-1.15; Al: < 0.1; Co ≤ 1.0; Ta ≤ 0.05; B ≤ 0.006; Mn ≤ 0.35; Si ≤ 0.35; P ≤ 0.015; S ≤ 0.015; C ≤ 0.08, all in wt.%) using WAAM based on gas metal arc welding.

A Yaskawa Motoman MA1440 industrial welding robot and a Fronius TPS500i power source, along with associated accessories, were utilized for the fabrication process. An Inconel 718 welding wire with a diameter of 1.2 mm served as the feedstock material. Deposition was carried out in a protective atmosphere of high-purity Argon (99.999%). The mechanical properties of the welding wire are listed in Table 1.

Table 1.

Mechanical properties of the welding wire

Welding wire material	Density, kg/m³	Young's modulus, GPa	Shear modulus G, GPa	Poisson's ratio
Inconel 718	8220	199	0.635	0.29

The robotic welding torch was maintained in an orientation perpendicular to the substrate plane throughout the entire deposition process. A stable material deposition process and optimal bead geometry were achieved with a torch travel speed of 40 cm/min and a wire feed speed of 4.5 m/min. To obtain the desired specimen width, transverse oscillations were applied to the torch, with a semi-amplitude of 7.0 mm and a frequency of 1.5 Hz. The resulting specimens had dimensions of 75 mm in length, 21 mm in width, and 25 mm in height (Fig. 1). The deposited layer thickness, under the selected WAAM process parameters (Table 2), was 1.1 ± 0.1 mm.

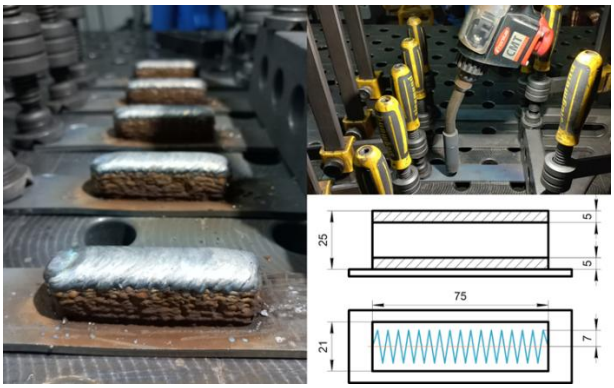

Fig. 1. Manufacturing technology of Inconel 718 alloy specimens using the WAAM method.

Before investigating the crystallographic texture, the specimens underwent grinding and chemical polishing (using a solution of 40 ml hydrochloric acid and 3 ml hydrogen peroxide) to a depth of up to 0.1 mm. This removed the surface layer affected by prior mechanical processing. θ-2θ scans were performed using a DRON-3M diffractometer with filtered Kα-Mo radiation and Bragg-Brentano geometry [18].

To investigate the anisotropy of elastic properties with respect to the deposition direction, prismatic specimens were extracted from the as-built blanks along two mutually orthogonal directions (Fig. 2).

Based on the scan data, IPFs were constructed for the X, Y, and Z directions of the specimens (designated as IPF X, IPF Y, and IPF Z, respectively). For the Z direction, scans were conducted on both the top and bottom surfaces, resulting in corresponding IPFs: IPF Z (top) and IPF Z (bottom). The IPFs were normalized according to the method described by Morris [19].

Pole density P_{hkl} is proportional to the ratio of the diffraction line intensity I_{hkl} in the textured specimen to the intensity of the corresponding line I_R in a texture-free specimen.

$$P_{hkl} = K\frac{I_{hkl}}{I_R}, \quad (1)$$

where the normalizing factor K according to Morris [18] is determined by the relationship:

$$K = \frac{1}{\sum_{\Delta} A_{hkl}(I_{hkl}/I_R)}, \quad (2)$$

where $\sum_{\Delta} A_{hkl} = 1$ n is the number of reflections. The values of coefficients $\{A_{hkl}\}$ are provided in the literature [20]. They account for the non-uniformity of the degree grid on the projection sphere, which increases the accuracy of pole density distribution on the IPF.

Thus, the pole density on the IPF is determined as:

$$P_{hkl} = \frac{I_{hkl}}{\sum_{\Delta} A_{hkl}(I_{hkl}/I_R)}. \quad (3)$$

II. Results and Discussion

Analysis of IPF Z (top) and IPF Z (bottom) (Fig. 3, a, b) of the grown specimen reveals that the maximum pole density is observed in the <310> pole (2.58 and 3.34, respectively) with pole density dispersion around the <100>, <931>, and <310> poles. The pole density in the <100> pole on IPF Z (bottom) (1.84) is lower than on IPF Z (top) (2.38), and the dispersion region is wider and captures the <311> pole. Additionally, on IPF Z (bottom), an increase in pole density is observed in the <332> pole (1.54) compared to IPF Z (top) (0.92). Such differences in the texture of the top and bottom surfaces of the grown specimen are likely due to the substrate's influence on the temperature conditions of the lower part of the deposited specimen.

From IPF X and IPF Y (Fig. 3, c, d), it is evident that the maximum pole density is observed in the <331> pole, but the magnitude of the maximum on IPF X (3.65) is greater than on IPF Y (3.13). The pole density dispersion on IPF X extends within a narrow band from the <331> pole to the <533> pole, in contrast to the wide dispersion region of pole density on IPF Y around the <331>, <311>, <100>, and <310> poles (Fig. 3, c, d). Such differences in texture along the X and Y directions may be attributed to the fact that in the Y direction, scanning was performed along the scanning direction during layer deposition, and in the X direction, accordingly, across it.

Analysis of the IPFs in Fig. 3 indicates that the crystallographic texture of the investigated Inconel 718 alloy specimen, grown using the aforementioned WAAM technology, can generally be described by a combination of ideal orientations {013} <331> + {001} <100> with the dispersion described above.

Table 2.

Main deposition parameters of the specimen fabrication process

Torch travel speed, cm/min	Wire feed speed, m/min	Current, A	Arc voltage, V	Shielding gas flow rate, l/min	Contact tip to work distance, mm
40.0±0.1	4.5±0.1	132.0±2.0	19.8±0.2	14.0±1.0	13.0±0.5

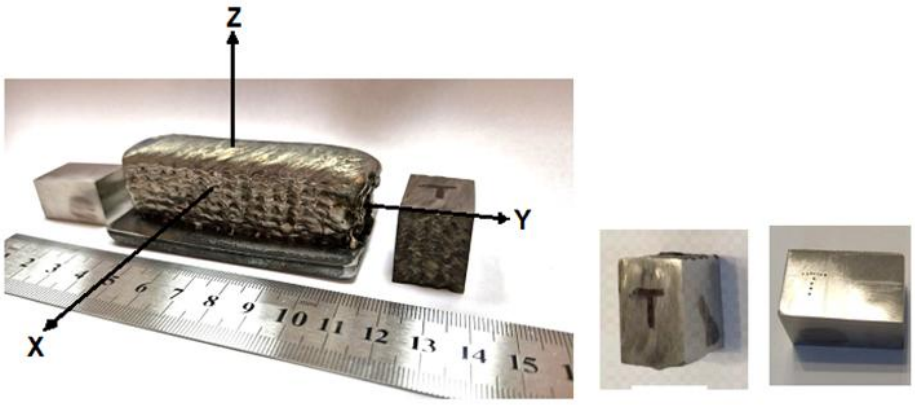

a b c

Fig. 2. Specimen of Inconel 718 alloy fabricated via WAAM technology (a) and specimens (b, c) after mechanical post-processing. The letter T on the specimen surface indicates the top surface.

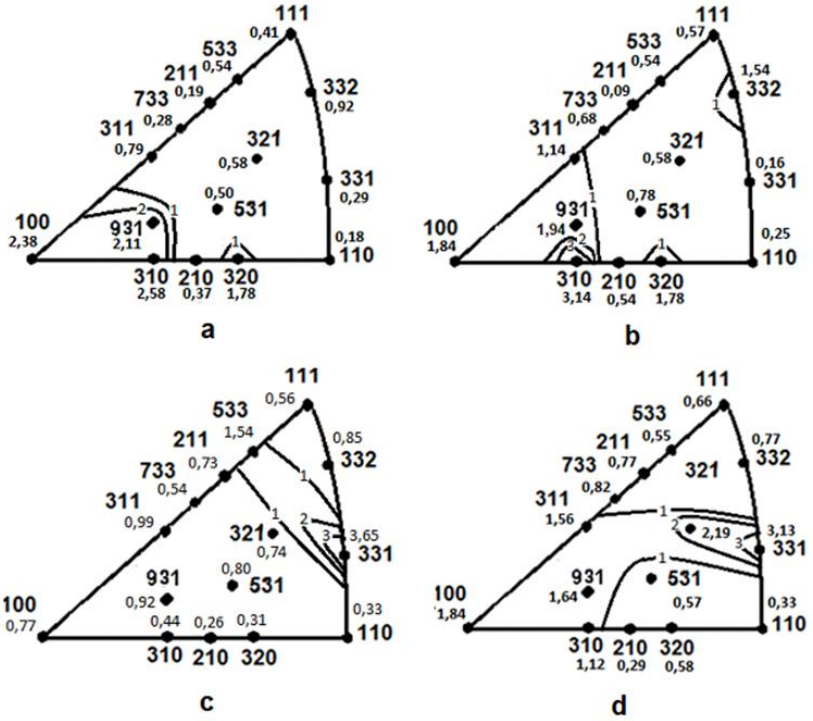

Fig. 3. Inverse pole figures of Inconel 718 alloy specimens obtained using WAAM technology: a - IPF Z (top); b - IPF Z (bottom); c - IPF X; d - IPF Y.

Multi-layer deposition causes heat accumulation during WAAM, which increases the preheating temperature of the previously created layer [21]. The Inconel 718 alloy has a low stacking fault energy (SFE) ≈ 0.75-0.80 mJ/m² [22, 23]. In alloys with low SFE, a texture of the aforementioned type may form during recrystallization [24]. The formation of cubic texture {001} <100>, as well as axial texture of type <100>‖ Z axis (see Fig. 2) during the growth of Inconel 718 alloy specimens using WAAM technology was observed in [25].

As is well-established, the pole density on an IPF (Fig. 3) is proportional to the volume fraction of crystals exhibiting the corresponding crystallographic orientation. Based on this principle, it is assumed that the effective elastic properties of the investigated polycrystalline specimens in a given direction can be represented as a weighted sum of the contributions from individual single crystals with corresponding orientations.

The weighting factor for each orientation is determined by the normalized pole density on the IPF corresponding to the specimen direction. This normalized pole density is calculated as the ratio of the pole density P_{hkl}^N to the sum of all determined pole densities, $\sum_{hkl} P_{hkl}$, on the respective IPF:

$$P_{hkl}^N = \frac{P_{hkl}}{\sum_{hkl} P_{hkl}}. \quad (4)$$

The Young's modulus, shear modulus, and Poisson's ratio of the investigated specimens were calculated using Miller indices ⟨hkl⟩ and elastic compliances and moduli of the single crystal of the investigated alloy [26, 27, 28].

The reciprocal value of the elastic modulus E of a single crystal is expressed through Miller indices ⟨hkl⟩ by the known relationship [26, 27]:

$$\frac{1}{E_{hkl}} = S_{11} - 2S_o\left(\frac{(hk)^2+(hl)^2+(lk)^2}{(h^2+k^2+l^2)^2}\right). \quad (5)$$

The reciprocal shear modulus of a single crystal is related to the direction ⟨hkl⟩ by the following formula [28]:

$$\frac{1}{G_{hkl}} = S_{44} + 4S_o\left(\frac{(hk)^2+(hl)^2+(lk)^2}{(h^2+k^2+l^2)^2}\right). \quad (6)$$

The Poisson's ratio of a single crystal in the direction ⟨hkl⟩ can be determined by the formula [26]:

$$\nu_{hkl} = \frac{1}{2} - \frac{E_{hkl}}{2(C_{11}+2C_{12})}. \quad (7)$$

In relationships (5) - (7), S_{ij} and C_{ij} – are the elastic compliances and elastic moduli of the single crystal, respectively; $S_0 = S_{11} + S_{12} - \frac{1}{2}S_{44}$; *hkl* – are the Miller indices of the corresponding poles on the IPF.

Considering the relationship expressed in equation (4), the effective elastic properties of the polycrystalline material can be determined as follows:

$$F_{poly}^{-1} = F_{hkl}^{-1}\, P_{hkl}^{N}, \quad (8)$$

where F is the corresponding property (E, G, or ν).

The values of elastic moduli of Inconel 718 alloy C_{ij} single crystals from various sources are presented in Table 3.

Further calculations were conducted using averaged results, as the figures vary significantly. Below are the mean values of elastic compliances of the Inconel 718 single crystal, obtained using established relationships [34] and information in Table 3:

$S_{11} = 0{,}007024144$ $(7{,}024 \cdot 10^{-12} Pa^{-1})$;

$S_{12} = -0{,}002600425$ $(-2{,}600 \cdot 10^{-12} Pa^{-1})$;

$S_{44} = 0{,}009208102$ $(9{,}208 \cdot 10^{-12} Pa^{-1})$;

$S_0 = S_{11} - S_{12} - 0{,}5 \times S_{44} = 0{,}005021$ $(5{,}021 \cdot 10^{-12} Pa^{-1})$

Normalized values of pole density on IPF (Fig. 2) were calculated using relationship (3).

Table 4 shows the calculation results for elastic modulus, shear modulus, and Poisson's ratio using relationships (5) - (8).

As shown in Table 4, the lowest calculated values of Young's modulus (187.5 and 190.3 GPa), and the highest values of shear modulus (84.3 and 83.3 GPa) and Poisson's ratio (0.329 and 0.327) correspond to the Z direction. The difference in Young's modulus values for Z (top) and Z (bottom) is insignificant and amounts to ≈ 1.5%, for shear modulus ≈ 1.2%, for Poisson's ratio ≈ 0.6%. This difference is likely associated with the substrate's influence on the temperature of the lower part of the specimen during its growth process.

The highest calculated values of Young's modulus (215.9 GPa) and, accordingly, the lowest shear modulus (74.2 GPa) and Poisson's ratio (0.303) correspond to the X direction (Table 4). In the Y direction, the calculated Young's modulus was 204.2 GPa, which is 5.4% less than in the X direction. Similarly, the shear modulus (78.2 GPa) and Poisson's ratio (0.303) are also less, by 5.2% and 3.5% respectively, than in the X direction. This is due to the fact that calculations of elastic properties in the Y direction were performed using texture characteristics obtained when scanning along the scanning direction, while calculations in the X direction were performed using texture data obtained by scanning across the scanning direction during the alloy layer deposition process (see Fig. 2 and Fig. 3, c, d).

Thus, the Young's modulus value calculated in the Z direction perpendicular to the alloy layer deposition direction using WAAM technology was found to be lower (by an average of 10-11%) than for the parallel deposition direction (X and Y). Meanwhile, the calculated values of shear modulus and Poisson's ratio were, conversely, higher. Similar trends were previously established when studying stainless steel specimens obtained using WAAM technology [35], as well as Inconel 718 alloy specimens

Table 3.

Elastic moduli of Inconel 718 alloy single crystal [in GPa]

No.	C_{11}	C_{12}	C_{44}	$C_0 = C_{ij} - C_{ij} - 2C_{ij}$	Source
1	284.0	127.0	87.0	–17.0	[[29]]
2	240.9	140.5	105.7	–111.0	[[30]]
3	259.6	179	109,6	–138.6	[[31]]
4	231.2	145.1	117,2	–148.3	[[32]]
5	244.8	149.2	123,6	–151.6	[[33]]
Average value	252.1	148.2	108,6	–113.3	

Table 4.

Calculated values of elastic properties of Inconel 718 alloy specimens

Calculation direction	Young's modulus, GPa	Shear modulus, GPa	Poisson's ratio
Z (top)	187.5	84.3	0.329
Z (bottom)	190.3	83.3	0.327
X	215.9	74.2	0.303
Y	204.2	78.2	0.314

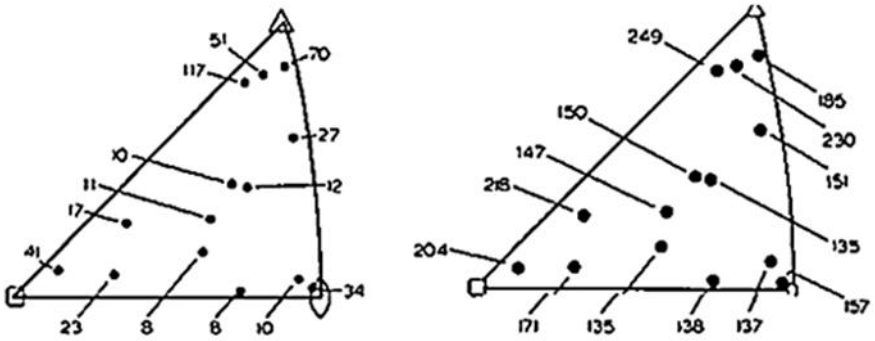

a b

Fig. 4. Strengthening coefficients (MPa) of 99.88% pure copper crystals at the first (a) and second (b) stages of strengthening for different orientations [37].

Table 5.

Mechanical properties of Inconel 718 alloy specimens obtained using WAAM technology

No.	UTS, MPa		YS, MPa		Elongation δ, %		Ref.
	X	Z	X	Z	X	Z	
1	774.8 ± 90	773.4 ± 25	537.2 ± 22	494.4 ± 25	13.5 ± 7	16.5 ± 5	[[39]]
2	684.0 ± 40	680 ± 90	622 ± 90	620 ± 20	8 ± 6	5 ± 3	[[40]]
3	760 766	753 513	440 482	498 332	45.6 41.4	39.0 41.4	[[40]]

obtained through selective laser sintering via 3D printing [36, 37].

The mechanisms of crystallographic texture formation in FCC metals and alloys after various types of deformation and subsequent heat treatment are fairly well understood [38]. Furthermore, crystallographic texture is one of the primary causes of anisotropy in mechanical properties. Analysis of deformation in FCC metal crystals has shown [38] that strengthening during deformation can vary widely depending on crystal orientation. Crystallites with orientations located near or on the edge of the [001]–[111] side of the stereographic triangle, toward which the tensile axis approaches during deformation, demonstrate greater strengthening than crystallites whose orientations lie in the central region of the stereographic triangle. Crystallites whose orientations are particularly distant from the [001]–[111] side prove to be less strong under tension.

As is known, the pole density on IPF (Fig. 3) is proportional to the volume fraction of crystals with the corresponding orientation. Based on the above, to predict the influence of crystal orientation on the strength properties of the investigated alloy specimens, one can use the value of the total pole density of crystal orientations along the [001]–[111] side of the stereographic triangle ($\sum_{[001]-[111]} P_{hkl}$) on the IPF taken in the X, Y, Z directions of the grown specimen. Analysis of the total pole density obtained on IPF X and IPF Y directions of the specimen, and on IPF Z-direction of the specimen showed that the total pole density of crystal orientations along [001]–[111] in the X and Y directions exceeds the corresponding value in the Z direction. The mechanisms of crystallographic texture formation in FCC metals and alloys after various types of deformation and subsequent heat treatment are fairly well understood [38]. Additionally, crystallographic texture is one of the main causes of anisotropy in mechanical properties. Analysis of deformation of FCC metal crystals has shown [38] that strengthening during deformation can vary widely depending on crystal orientation. Crystallites with orientations located near or on the edge of the [001]–[111] side of the stereographic triangle, toward which the tensile axis approaches during deformation, demonstrate greater strengthening than crystallites whose orientations lie in the central region of the stereographic triangle. Crystallites whose orientations are particularly distant from the [001]–[111] side prove to be less strong under tension. The greatest strengthening was found in crystals with [001] and [111] orientations, both in the first and second stages of strengthening, although not as pronounced (Fig. 4) [38].

Thus, the total pole density on
IPF X $\sum_{[001]-[111]} P_{hkl}$ = 5.13,
on IPF Y $\sum_{[001]-[111]} P_{hkl}$= 6.20, and the value averaged over IPF Z (top) and
IPF Z (bottom) $\sum_{[001]-[111]} P_{hkl}$ = 4.86. It can be expected that as a result, the strength properties of the specimen obtained using WAAM technology in the X and Y directions may be higher, and accordingly, the plastic characteristics lower, than in the Z direction.

Analysis of literature regarding the mechanical properties of Inconel 718 alloy specimens manufactured using WAAM technology showed that the above statement is correct (Table 5).

This indicates that crystallographic texture is one of the main causes of anisotropy in the characteristics of the investigated Inconel 718 alloy specimens. Therefore, by rationally utilizing the crystallographic texture of specimens obtained using WAAM technology in the corresponding specimen directions, it is possible to manufacture components with an optimal set of qualities.

Conclusions

The crystallographic texture of Inconel 718 alloy

specimens synthesized using Wire Arc Additive Manufacturing (WAAM) technology has been investigated using inverse pole figures (IPF). The crystallographic texture was examined by the inverse pole figures method in three orthogonal directions of the specimens: layering (X), scanning (Y), and the direction perpendicular to them (Z).

Based on the diffraction analysis results, it has been established that the texture of the investigated specimens can be characterized by a combination of ideal orientations (013)[3$\bar{3}$1]+(001)[100] with a certain degree of dispersion. The formation of the revealed texture is conditioned by recrystallization processes occurring due to significant thermal influence during the layer-by-layer growth of Inconel 718 alloy specimens using the WAAM technology.

A comprehensive assessment of the anisotropy of mechanical properties of the material has been carried out based on experimentally determined elastic constants of single crystals of the investigated alloy and quantitative characteristics of pole density on inverse pole figures. Specifically, the values of Young's modulus, shear modulus, and Poisson's ratio have been calculated in three mutually perpendicular directions of Inconel 718 alloy specimens after their manufacturing using WAAM technology and subsequent post-processing.

It has been experimentally established that the Young's modulus value in the Z direction, perpendicular to the material layering plane during additive manufacturing using WAAM technology, demonstrates a statistically significant reduction (by an average of 10-11%) compared to similar indicators calculated for directions parallel to the deposition plane (X and Y). At the same time, the calculated values of shear modulus and Poisson's ratio in the Z direction are characterized by the opposite tendency, demonstrating increased values relative to the XY plane. Similar patterns of anisotropy in elastic properties were previously identified when studying specimens of Inconel 718 superalloy obtained using the alternative technology of selective laser sintering (SLS) with additive 3D printing.

The conducted quantitative texture analysis revealed that the integral pole density along the crystallographic diagonal [001]–[111] of the stereographic triangle on the inverse pole figures of the X and Y directions of the investigated specimens significantly exceeds the corresponding parameter on the IPF of the Z direction. The established correlation between pole density distribution and anisotropy of elastic characteristics creates a methodological basis for predictive assessment of mechanical properties of Inconel 718 alloy products manufactured using WAAM technology. The reliability of the proposed approach is confirmed by the results of comparative analysis of quantitative texture characteristics and corresponding mechanical properties obtained from literature sources for similar materials.

The obtained results have important practical significance for predicting the mechanical behavior of structural elements made of this alloy under various loading schemes and can be used in developing optimized modes of additive manufacturing of components for critical applications.

Acknowledgment

The work was performed with the support of NRFU (project No. 2023.04/0098 "Development of practical recommendations for expanding the application of additive manufacturing technologies for parts production and field repair of military equipment", 0124U003918).

Usov V.V. – Doctor of physical and mathematical science, Professor, Professor of the department of technological and vocational education;
Shkatulyak N.M. – Candidate of Physical and Mathematical Sciences, Associate Professor, Associate Professor of the Department of Applied Mathematics and Computer Science;
Iovchev S.I. – Candidate of Physical and Mathematical Sciences, Associate Professor of the Department of "Ship Electrical Power Engineering, Physics, Operation of Electrical Equipment";
Pavlenko D.V. – Doctor of Technical Sciences, Professor, Head of the Department of Aircraft Engine Technology;
Molochkov D.E. – Senior Lecturer, Department of Information Technology and Electronic Media;
Kulikovsky R.A. – Candidate of Technical Sciences, Associate Professor.

[1] D. Pavlenko, Y. Dvirnyk, & R. Przysowa, *Advanced materials and technologies for compressor blades of small turbofan engines.* IOP Conference Series: Materials Science and Engineering, 1024(1), 012061 (2021); https://doi.org/10.1088/1757-899X/1024/1/012061.
[2] L.P. Raut, R.V. Taiwade, *Wire Arc Additive Manufacturing: A Comprehensive Review and Research Directions*, J. Mater. Eng. Perform. 30, 4768 (2021);. https://doi.org/10.1007/s11665-021-05871-5.
[3] ISO/ASTM 52900:2021(en) Additive manufacturing – General principles – Fundamentals and vocabulary. https://www.iso.org/obp/ui/#iso:std:iso-astm:52900:ed-2:v1:en.
[4] D.G. Ahn, *Directed Energy Deposition (DED) Process: State of the Art. Int*. J. of Precis. Eng. and Manuf.-Green Tech. 8, 703 (2021); https://doi.org/10.1007/s40684-020-00302-7.
[5] Saboori Abdollah, Alberta Aversa, Giulio Marchese, Sara Biamino, Mariangela Lombardi, and Paolo Fino. *Application of Directed Energy Deposition-Based Additive Manufacturing in Repair*, Applied Sciences, 9(16); 3316 (2019); https://doi.org/10.3390/app9163316.
[6] RAMLAB. WAAM 101. https://www.ramlab.com/resources/waam-101/#down
[7] M.N. Mahdi, A.R. Ahmad, H. Natiq, M.A. Subhi, & Q.S. Qassim, *Comprehensive Review and Future Research Directions on Dynamic Faceted Search.* Applied Sciences, 11(17), 8113 (2020); https://doi.org/10.3390/app11178113.

[8] K. Amato, S. Gaytan, L. Murr, E. Martinez, P. Shindo, J. Hernandez, S. Collins, & F. Medina, *Microstructures and mechanical behavior of Inconel 718 fabricated by selective laser melting*. Acta Materialia, 60(5), 2229 (2012); https://doi.org/10.1016/j.actamat.2011.12.032.

[9] X. Xu, J. Ding, S. Ganguly, & S. Williams, *Investigation of process factors affecting mechanical properties of INCONEL 718 superalloy in wire + arc additive manufacture process*. Journal of Materials Processing Technology, 265, 201 (2019); https://doi.org/10.1016/j.jmatprotec.2018.10.023.

[10] C. Fuchs, D. Baier, T. Semm et al. *Determining the machining allowance for WAAM parts*. Prod. Eng. Res. Devel. 14, 629 (2020); https://doi.org/10.1007/s11740-020-00982-9.

[11] Y. Manurung, K.P. Prajadhiana, M.S. Adenan et al., *Analysis of material property models on WAAM distortion using nonlinear numerical computation and experimental verification with P-GMAW*. Archiv.Civ.Mech.Eng 21, 32 (2021); https://doi.org/10.1007/s43452-021-00189-4.

[12] S.R. Singh & P. Khanna, *Wire arc additive manufacturing (WAAM): A new process to shape engineering materials.* Materials Today: Proceedings, 44, 118 (2020); https://doi.org/10.1016/j.matpr.2020.08.030.

[13] V. Laghi et al., *Experimental results for structural design of Wire-and-Arc Additive Manufactured stainless steel members*, Journal of Constructional Steel Research. 167, 1 (2019); https://doi.org/10.1016/j.jcsr.2019.105858.

[14] N. Hadjipantelis, B. Weber, C. Buchanan, L. Gardner, *Description of anisotropic material response of wire and arc additively manufactured thin-walled stainless steel elements*. Thin-Walled Structures. 171,108634 (2022); https://www.researchgate.net/publication/354300686_Characterisation_of_the_anisotropic_response_of_wire_and_arc_additively_manufactured_stainless_steel.

[15] P. Kyvelou, H. Slack, D. Daskalaki Mountanou, M.A. T. Wadee Britton Ben, C. Buchanan, L. Gardner *Mechanical and microstructural testing of wire and arc additively manufactured sheet material*. Materials and Design. 192, 108675 (2020); https://www.sciencedirect.com/science/article/pii/S0264127520302094?via%3Dihub.

[16] L. Zhang, R. Barrett, P. Cloetens, C. Detlefs, and M. Sanchez del Rio, *Anisotropic elasticity of silicon and its application to the modelling of X-ray optics*, J. of Synchrotron Radiation.21 (3), 507 (2014); https://doi.org/10.1107/S1600577514004962.

[17] P. Kyvelou, H. Slack, D. Daskalaki Mountanou, M.A. Wadee, T.B. Britton, C. *Buchanan, & L. Gardner, Mechanical* and microstructural testing of wire and arc additively manufactured sheet material. Materials & Design, 192, 108675 (2020); https://doi.org/10.1016/j.matdes.2020.108675.

[18] Instrument X-ray Optics: Reflection Geometry. URL: http://pd.chem.ucl.ac.uk/pdnn/inst1/optics1.htm.

[19] P.R. Morris, *Reducing the Effects of Nonuniform Pole Distribution in Inverse Pole Figure Studies*. Journal of Applied Physics, 30, 595 (1959); https://aip.scitation.org/doi/10.1063/1.1702413.

[20] Ya.D. Vishnyakov, Teoriya Obrazovaniya Tekstur v Metallakh i Splavakh [The Theory of Texture Formation in Metals and Alloys] (Moskva: Nauka: 1979) (in Russian)

[21] S. Singh, I.A. Palani, C.P. Paul, A. Funk, & P.K. Gokuldoss, *Wire Arc Additive Manufacturing of NiTi 4D Structures: Influence of Interlayer Delay*. 3D Printing and Additive Manufacturing, 11(1), 152 (2024); https://doi.org/10.1089/3dp.2021.0296.

[22] M. Sundararaman, P. Mukhopadhyay, & S. Banerjee, *Deformation behaviour of γ" strengthened inconel 718*. Acta Metallurgica, 36(4), 847 (1988); https://doi.org/10.1016/0001-6160(88)90139-3.

[23] P. Patra, S. Dey, N. Gayathri, & P. Mukherjee, *Influence of alloying elements on stacking fault energy in Ni and Ni-based alloy: A first–principles study*. Computational and Theoretical Chemistry, 1240, 114815 (2024); https://doi.org/10.1016/j.comptc.2024.114815.

[24] J. Slakhorst, *The development of recrystallization textures in F.C.C. Metals with a low stacking fault energy*. Acta Metallurgica, 23(3), 301 (1975); https://doi.org/10.1016/0001-6160(75)90122-4.

[25] B. Lan, Y. Wang, Y. Liu, P. Hooper, C. Hopper, G. Zhang, X. Zhang, & J. Jiang, *The influence of microstructural anisotropy on the hot deformation of wire arc additive manufactured (WAAM) Inconel 718*. Materials Science and Engineering: A, 823, 141733 (2021); https://doi.org/10.1016/j.msea.2021.141733.

[26] P. Aba-Perea, T. Pirling, P. Withers, J. Kelleher, S. Kabra, & M. Preuss, *Determination of the high temperature elastic properties and diffraction elastic constants of Ni-base superalloys*. Materials & Design, 89, 856 (2016); https://doi.org/10.1016/j.matdes.2015.09.152.

[27] J. Everaerts, C. Papadaki, W. Li, & A.M. Korsunsky, *Evaluation of single crystal elastic stiffness coefficients of a nickel-based superalloy by electron backscatter diffraction and nanoindentation*. Journal of the Mechanics and Physics of Solids, 131, 303 (2019); https://doi.org/10.1016/j.jmps.2019.07.011.

[28] L. Zhang, R. Barrett, P. Cloetens, C. Detlefs, & M. Sanchez del Rio, *Anisotropic elasticity of silicon and its application to the modelling of X-ray optics.* Journal of Synchrotron Radiation, 21(3), 507 (2014); https://doi.org/10.1107/S1600577514004962.

[29] T. Obermayer, C. Krempaszky, and E. Werner, *Analysis of texture and anisotropic elastic properties of additively manufactured Ni-base alloys*. Metals. 12(11), 1991 (2022); https://doi.org/10.3390/met12111991.

[30] P. Haldipur, F.J. Margetan, and R.B. Thompson, *Estimation of single-crystal elastic constants from ultrasonic measurements on polycrystalline specimens*. AIP Conf. Proc. 700(1), 1061 (2004); https://doi.org/10.1063/1.1711735.

[31] G. Martin, N. Ochoa, K. Sai, E. Hervé-Luanco, and G. Cailletaud, *A multiscale model for the elastoviscoplastic behavior of directionally solidified alloys: application to FE structural computations*, Int. J. of Solids and Struct. 51(5), 1175 (2014); https://doi.org/10.1016/j.ijsolstr.2013.12.013.

[32] S. Jothi, S. V. Merzlikin, T. N. Croft, J. Andersson, and S. G. R. Brown, *An investigation of micro-mechanisms in hydrogen induced cracking in nickel-based super-alloy 718,* J. of Alloys and Compounds. 664, 664 (2016); https://doi.org/10.1016/j.jallcom.2016.01.033.

[33] P. Aba-Perea, T. Pirling, P. Withers, J. Kelleher, S. Kabra, and M. Preuss, *Determination of the high temperature elastic properties and diffraction elastic constants of Ni-base superalloys*, Materials & Design. 89(5), 856 (2016); https://doi.org/10.1016/j.matdes.2015.09.152.

[34] J.F. Nye, *Physical Properties of Crystals: Their Representation by Tensors and Matrices*. Oxford: Clarendon Press, 322 (1985); https://vdoc.pub/download/physical-properties-of-crystals-their-representation-by-tensors-and-matrices-3ib3oss7ne9g.

[35] V. Laghi, L. Tonelli, M. Palermo, M. Bruggi, R. Sola, L. Ceschini, & T. Trombetti, *Experimentally-validated orthotropic elastic model for Wire-and-Arc Additively Manufactured stainless steel*. Additive Manufacturing, 42, 101999 (2021); https://www.sciencedirect.com/science/article/abs/pii/S2214860421001640.

[36] V.V. Usov, N.M. Shkatuliak, D.V. Pavlenko, et al., *Anisotropy of Elastic Properties of Inconel 718 Alloy Specimens Obtained by 3D Printing*. Mater Sci, 59, 414 (2023); https://doi.org/10.1007/s11003-024-00792-9.

[37] K. Kunze, T. Etter, J. Grässlin, & V. Shklover, *Texture, anisotropy in microstructure and mechanical properties of IN738LC alloy processed by selective laser melting (SLM).* Materials Science and Engineering: A, 620, 213 (2015); https://doi.org/10.1016/j.msea.2014.10.003.

[38] R.V.K. Honeycombe, *The Plastic Deformation of Metals*. London: Edward Arnold Ltd. Publ.: (1984); https://archive.org/details/plasticdeformati0000hone_c4v2/page/n5/mode/2up?view=theater.

[39] U. Alonso, F. Veiga, A. Suárez, & A. Gil Del Val, *Characterization of Inconel 718® superalloy fabricated by wire Arc Additive Manufacturing: Effect on mechanical properties and machinability*. Journal of Materials Research and Technology, 14, 2665 (2021); https://doi.org/10.1016/j.jmrt.2021.07.132.

[40] T. Bhujangrao, F. Veiga, A. Suárez, E. Iriondo, & F.G. Mata, *High-Temperature Mechanical Properties of IN718 Alloy: Comparison of Additive Manufactured and Wrought amples*. Crystals, 10(8), 689. (2020); https://doi.org/10.3390/cryst10080689.

[41] V. Santhosh, N. Babu, *A Study on Microstructure and Mechanical Properties of Inconel 718 Superalloy Fabricated by Novel CMT-WAAM Process*. Materials Research, 27, e20230258 (2024; https://doi.org/10.1590/1980-5373-MR-2023-0258.

В.В. Усов[1], Н.М. Шкатуляк[1], С.І. Іовчев[2], Д.В. Павленко[3], Д.Е. Молочков[3], Р.А. Куликовський[3]

Анізотропія пружних властивостей у зразках зі сплаву Inconel 718, виготовлених методом електродугового адитивного виробництва

[1]Південноукраїнський національний педагогічний університет імені К. Д. Ушинського, Одеса, Україна;
[2]Одеський національний морський університет, Одеса, Україна;
[3]Національний університет «Запорізька політехніка», Запоріжжя, Україна, dvp1977dvp@gmail.com

Досліджено анізотропію пружних властивостей зразків зі сплаву Inconel 718, отриманих за технологією адитивного виробництва з використанням дротяної дуги (WAAM). Вивчено кристалографічну текстуру зразків методом обернених полюсних фігур, знятих у трьох взаємно перпендикулярних напрямках: у напрямку складання шарів, напрямку сканування і перпендикулярному до них напрямку. Встановлено, що текстура може бути описана комбінацією ідеальних орієнтировок з розсіянням. На основі констант пружності монокристалів сплаву та даних полюсної густини на обернених полюсних фігурах, оцінено модуль Юнга, модуль зсуву і коефіцієнт Пуассона у трьох взаємно перпендикулярних напрямках. Виявлено, що величина модуля Юнга у напрямку, перпендикулярному напрямку складання шарів, нижча (в середньому на 10-11%) порівняно з паралельними напрямками, тоді як значення модуля зсуву та коефіцієнта Пуассона, навпаки, вищі. Показано, що кристалографічна текстура є основною причиною анізотропії механічних властивостей досліджуваних зразків. Раціональне використання кристалографічної текстури при виготовленні зразків за технологією WAAM дозволяє отримати деталі з оптимальним поєднанням механічних характеристик.

Ключові слова: дротяно-дугове адитивне виробництво, кристалографічна текстура, жароміцний сплав Inconel 718, інверсні полюсні фігури, анізотропія.